Investigation of magnetization dynamics in trilayer width-modulated nanowires

Mahathi Kuchibhotla ; Arabinda Haldar ✉ ; Adekunle Olusola Adeyeye ✉

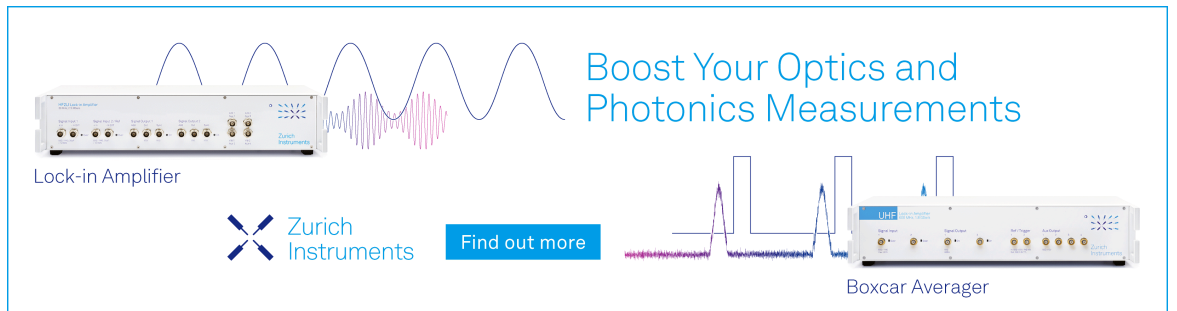Check for updates

CrossMark

View Online

Export Citation

22 March 2024 09:32:59

Journal of Applied Physics

AIP Publishing

Investigation of magnetization dynamics in trilayer width-modulated nanowires

Mahathi Kuchibhotla,[1] 🆔 Arabinda Haldar,[1,a)] 🆔 and Adekunle Olusola Adeyeye[2,3,a)] 🆔

AFFILIATIONS

[1]Department of Physics, Indian Institute of Technology Hyderabad, Kandi 502284, Telangana, India
[2]Information Storage Materials Laboratory, Department of Electrical and Computer Engineering, National University of Singapore, Singapore 117576
[3]Department of Physics, Durham University, South Road, Durham, DH1 3LE, United Kingdom

[a)]Authors to whom correspondence should be addressed: arabinda@phy.iith.ac.in and adekunle.o.adeyeye@durham.ac.uk

ABSTRACT

We have investigated the magnetization reversal processes and dynamic behavior of trilayered $Py(50\,nm)/Pd(t_{Pd})/Py(20\,nm)$ nanowires with periodic width modulation as a function of spacer layer thickness t_{Pd} in the range from 0 to 10 nm and compared them with single-layer nanowires. The ferromagnetic resonance spectra show more than three modes that result from a non-uniform demagnetizing field in width-modulated nanowires. We observe that the spacer layer thickness influenced the ferromagnetic resonance spectra, which showed different numbers and values of modes and frequencies due to the different magnetization configurations for different spacer layer thicknesses. We also found that the two ferromagnetic layers are exchange-coupled for $t_{Pd} = 2\,nm$ nanowire arrays, showing the sharp switching of magnetization from the static measurements and sharp frequency jump from 13.6 to 14.7 GHz around $-18\,mT$ from the dynamic measurements. However, for $t_{Pd} = 10\,nm$, the two layers switch at different fields, indicating a gradual decrease in magnetization as the reversal is mediated through dipolar coupling. The origin of modes is well explained from the spatial mode profiles of top and bottom magnetic layers. The dynamic responses in this spin-valve-type structure are useful for designing microwave-based spintronic devices.

INTRODUCTION

Magnonics is a blossoming sub-field of spintronics that employs the excitation of magnetic materials called spin waves or magnons to carry, store, and process information in magnetic nanostructures.[1–3] Utilizing spin waves as data carriers offers advantages, including low power consumption, reconfigurability, high-frequency operation, miniaturization, and compatibility with existing complementary metal-oxide semiconductor (CMOS) technology.[4] Research on magnonics in recent years has unravelled the fundamental physics to introduce prototype devices such as transistors, oscillators, filters, and logic gates.[5–9] These inventions of magnonic devices have fueled the demand for the design of various synthetic reconfigurable magnonic crystals (MCs) to control spin waves.[10] The MCs are magnetic metamaterials consisting of periodic nanomagnets and exhibit rich, dynamic spectra possessing magnonic bandgaps.[11–15]

A nanowire array represents a fundamental example of a one-dimensional magnonic crystal, wherein shape anisotropy facilitates the alignment of magnetization along the wire's length, independent of an external magnetic field.[16] These act as waveguides to carry information encrypted in spin waves for applications in spintronic devices.[17,18] Recently, investigations have been carried out on magnetization reversal and collective magnetization dynamics in planar nanowires. Here, the microwave properties lying in the GHz regime are tuned as a function of thickness, lateral dimensions, magnetic field amplitude, and orientation.[19–24] The ease of fabrication techniques has opened up a way to explore multilayer systems (three-dimensional MCs). These have spin-valve-type architecture and exhibit exotic properties such as spin pumping, giant magneto-resistance, and interlayer coupling.[25–27] The dipolar and exchange coupling fields give additional functionalities to engineer the spin wave spectra in multilayer systems.[28,29] The impact of magnetization orientation (i.e., the layers are exchanged or dipolar coupled) in the multilayers on the magnetization reversal and dynamical properties is studied.[30] The spin waves are probed using the

Brillouin light scattering technique to detect the propagation properties (stationary or dispersive) and bandwidths of the detected modes.[31,32] Thinking beyond the planar wire with homogeneous width, modified shape anisotropy at the modulated regions in the wire is being exploited to tune the resonant spectra.[33,34] The width-modulated regions act as pinning sites, offering a route for designing reprogrammable resonant spectra.[35] Previous works mainly focused on single-layer width-modulated nanowires (WMNWs).[36,37] However, studying multilayer's magnetization reversal and dynamic properties is limited only to regular wires with no width modulation.

Here, we report the role of dipole and exchange coupling on magnetization reversal processes and spin dynamics in WMNW arrays consisting of two ferromagnetic (Py–$Ni_{80}Fe_{20}$) layers separated by a non-magnetic palladium (Pd) spacer layer, i.e., Py (50 nm)/Pd(t_{Pd})/Py(20 nm). In this respect, two different thicknesses (t_{Pd} = 2 and 10 nm) of the spacer layer have been explored. The results are compared with nanowires with no spacer layers [i.e., t_{Pd} = 0 nm or a single layer of Py(70 nm)] and the constituent individual single-layer nanowires [i.e., Py(50 nm) and Py(20 nm)]. A single-step magnetization reversal is observed for t_{Pd} = 0 and 2 nm, accounting for the presence of exchange coupling between the layers for t_{Pd} = 2 nm. Meanwhile, t_{Pd} = 10 nm shows two-step distinct switching as the top and bottom layers reverse magnetization at different fields due to the dipolar coupling between them. Ferromagnetic resonance (FMR) spectra of WMNW arrays are sensitive to the spacer layer thickness, field amplitude, and orientation. Micromagnetic simulations are performed to provide insights into the experimental observations.

EXPERIMENTAL AND SIMULATION DETAILS

The single and trilayer Permalloy nanowire arrays with continuous width modulation are fabricated over a large area of 4×4 mm^2 using a deep ultraviolet (DUV) lithography technique at an exposure wavelength of 193 nm. The thicknesses of single-layer Py are 20 and 50 nm. The trilayer WMNW arrays consist of two Py layers separated by a Pd spacer, i.e., Py(50 nm)/Pd(t)/Py(20 nm). The thicknesses of the bottom and top Py layers are fixed at 50 and 20 nm, respectively, and the thicknesses of the spacer layer t_{Pd} are 0, 2, and 10 nm. The patterning of WMNW arrays is followed by the deposition of Py films on top of a Cr (5 nm) adhesive layer using electron beam deposition. Two control samples with 20-nm-thick and 50-nm-thick single-layer nanowires are also fabricated for comparison. Thin film deposition is performed in a vacuum chamber with a base pressure of less than 5×10^{-8} Torr and a deposition rate of 0.2 Å/s. The lift-off process follows this after soaking the samples in a DUV resist removal solution (OK 73 resist thinner). The details of the fabrication process are described elsewhere.[38] The collective magnetization reversal processes of the arrays of WMNW structures are probed at room temperature using a vibrating sample magnetometer (VSM) by applying an in-plane external field along the easy and hard axes of the WMNW arrays. The magnetization dynamics of the WMNW samples are measured using a lock-in-based broadband FMR experimental setup at room temperature. The samples are mounted in flip-chip style on the ground-signal-ground (GSG) type coplanar waveguide (CPW). The

CPW connected to the microwave generator sends the microwave signal, which generates the excitation field (h_{rf}) perpendicular to the applied field to excite magnetization. The FMR spectra are measured by sweeping the excitation frequency of h_{rf} from 2 to 18 GHz while maintaining a constant bias field (H_{app}). In this work, H_{app} is varied from +300 to −300 mT. The in-plane angular measurements are performed by rotating the sample to vary the field orientation (θ) from 0° to 360° with a step of 15°. The FMR records the derivative of the absorption power (dP/dH_{app}) as a function of H_{app}. An alternating current source connected to a pair of Helmholtz coils is used to modulate H_{app} at a reference frequency of 490 Hz, and the data are recorded at the reference frequency.

Micromagnetic simulations are performed using MuMax3, which is an open-source micromagnetic simulation software to understand the magnetization reversal processes and dynamic responses and validate with experimental results.[39] The material parameters of Py used in the simulation are saturation magnetization (M_s) = 8×10^5 A/m, exchange constant (A) = 13×10^{-12} J/m, damping constant (α) = 0.008, magnetocrystalline anisotropy (K) = 0. The sample in the simulation is discretized into cells of size $5 \times 5 \times 2$ nm^3. The cell size (≤ 5 nm) is chosen to be smaller than the exchange length of Py defined by $l_{ex} = \sqrt{\frac{2A}{M_s^2\mu_0}}$ (=5.7 nm) to neglect the exchange interactions within the cell. The equilibrium magnetization states are computed by solving the Landau–Lifshitz–Gilbert (LLG) equation with a large value of α = 0.5.[40] The sample is saturated by applying $\mu_0 H_{app}$ of 200 mT along the easy axis of the nanowire, and the hysteresis loops are recorded by sweeping the field with a field step of 2 mT. The dynamic simulations are performed by applying a *sinc* magnetic field defined as $h_{rf} = h_0 \frac{\sin(2\pi f_c \tau)}{2\pi f_c \tau}$, perpendicular to the film plane to obtain maximum excitation efficiency. Here, the amplitude of *sinc* wave $\mu_0 h_0$ = 5 mT, cut-off frequency f_c = 19 GHz and $\tau = t - t_0$ refers to the simulation time (t) with an offset t_0. The time domain simulations are performed for 4 ns at 10 ps time step, and the magnetization as a function of x, y, z, and t is recorded. The magnetization data as a function of time are Fourier transformed to obtain FMR response in the frequency domain. The spatial distribution of modes are obtained by carrying out spatial fast Fourier transform (FFT) on $M(x,y,z,t)$.[40]

RESULTS AND DISCUSSION

Field-emission scanning electron microscopy (FESEM) is used to inspect the quality of the samples. All the nanowires are of good quality with clear modulation in width. For illustration, the FESEM image of trilayer WMNW with t_{Pd} = 10 nm is shown in Fig. 1(a). The width of the widest region is 235 nm, and the narrowest region is 150 nm. The wires are arranged in a periodic array with a period of 600 nm. Therefore, the wires are magnetically decoupled from each other. The schematic of the CPW in the FMR setup is shown in Fig. 1(b).

MAGNETIZATION REVERSAL PROCESSES

To understand the magnetization reversal processes in trilayer WMNW arrays, we have measured hysteresis loops as a function of t_{Pd}. The hysteresis loops for the H_{app} along the easy and hard axes
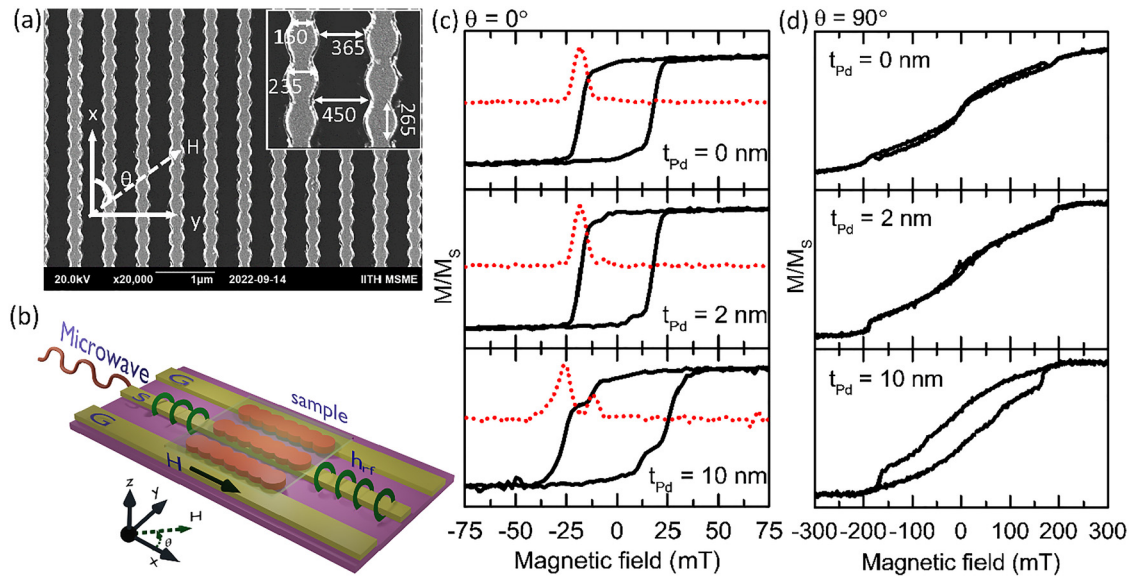
FIG. 1. (a) FESEM image of trilayer WMNW array with t_{Pd} = 10 nm. Lateral dimensions are indicated in the inset. (b) Sketch of the G-S-G CPW of the FMR set up with a sample placed in the flip-chip configuration on the top of CPW. Hysteresis loops of trilayer WMNW arrays with t_{Pd} = 0 nm, t_{Pd} = 2 nm, and t_{Pd} = 10 nm for (c) θ = 0° and (d) θ = 90°. On the same graph, we show the red dotted curve as dM/dH_{app} in arbitrary units.

of the wire are shown in Figs. 1(c) and 1(d). The hysteresis loops are markedly sensitive to the field orientation and t_{Pd}. The drastic change in the coercive field (μ_0H_c) with the change in the field orientation is due to the strong shape anisotropy along the easy axis of the nanowire.

In contrast, the modification of the magnetization reversal process with a change in t_{Pd} is ascribed to the different coupling mechanisms between the two ferromagnetic layers. First, we discuss the hysteresis loops and corresponding dM/dH_{app} curves for the case of θ = 0°, as shown in Fig. 1(c). For the 70-nm-thick single-layer nanowires (i.e., for t_{Pd} = 0 nm), the hysteresis loop indicates the presence of sharp switching of magnetization with μ_0H_c around 17.6 mT and a single peak in the dM/dH_{app} curve. The sharpness of the switching is calculated from the squareness ratio, defined as the ratio between remanent magnetization and saturation magnetization. The squareness ratio for a nanowire with no modulation in width is ~1, whereas it is ~0.89 in the WMNW array with t_{Pd} = 0 nm. This is because the magnetization switching at the modulated region and bulk part of the nanowire does not occur at the same magnetic field. A comparatively larger magnetic field is required to reverse magnetization in the constricted regions. The hysteresis loop for t_{Pd} = 2 nm also shows a similar behavior as that of the case in t_{Pd} = 0 nm with μ_0H_c of ~17.6 mT. Hence, the exchange coupling between the two ferromagnetic layers dominates the magnetization reversal process. However, a small peak in the dM/dH_{app} curve is found at −7.2 mT in addition to the large intense peak at −18 mT. This indicates the onset of the non-parallel alignment between the ferromagnetic layers. Since the peak is less intense, the whole volume of the thin layer is not independently switched. However, this behavior is more pronounced in the case

of t_{Pd} = 10 nm, where the top and bottom ferromagnetic layers are exchange decoupled. Hence, the dipolar coupling plays an important role in the reversal mechanism. The hysteresis loop, corresponding to t_{Pd} = 10 nm, shows gradual switching corresponding to the independent switching of the top and bottom layers. In the case of t_{Pd} = 10 nm, μ_0H_c is 24 mT, which is ~6 mT greater than that of WMNW arrays with t_{Pd} = 0 nm and t_{Pd} = 2 nm. This difference in μ_0H_c indicates the variation in the coupling mechanism. The two distinct peaks in the dM/dH_{app} curve at −26 and −12 mT represent the switching fields of the bottom [Py(50)] and top [Py(20)] layers, respectively. In this field range, the magnetizations of the top and bottom layers are in non-parallel alignment. Thus, the change in behavior of the hysteresis loop from sharp to less sharp, switching with an increase in the spacer layer thickness, indicates a transition from exchange-dominated to dipolar coupling between the ferromagnetic layers.

To obtain a detailed picture of the reversal process, we have simulated the hysteresis loops for t_{Pd} = 0, 2, and 10 nm WMNW arrays (see Fig. S1 in the supplementary material for more information). We have found that μ_0H_c increases with an increase in t_{Pd}, which aligns with the experimental results. Now, we discuss the hysteresis loops measured at θ = 90° as shown in Fig. 1(d). A drastic change in the shape of the hysteresis loops is observed for θ = 90°. A large μ_0H_{app} of ~200 mT is required to saturate the nanowires along the hard axis direction. This is because of an increase in the demagnetizing field when H_{app} deviates from the easy axis direction. The magnetization tries to align in the easy axis direction when the field is reduced below the saturation field. Therefore, negligible coercivity is seen in the case of θ = 90°. Interestingly, non-monotonic change in μ_0H_c is observed with an

increase in the thickness of the single-layer nanowires from 20 to 70 nm (see Fig. S2 in the supplementary material for more information).

MICROWAVE PROPERTIES IN TRILAYER WIDTH-MODULATED NANOWIRES

Next, we investigate the effect of the different interlayer coupling mechanisms on spin dynamics in all the arrays, including control samples with single-layer nanowire arrays. Figure 2(a) shows the experimental FMR spectra at $\mu_0 H_{app} = 0$ mT for $\theta = 0°$

for the trilayer WMNW arrays at different t_{Pd} values. From the hysteresis loops [Fig. 1(c)], it is clear that magnetization lies along the easy axis of the nanowire at remanence. Thus, we observe the Kittel-like modes even in the absence of the field, which can be understood by using the Kittel equation,

$$f = \frac{\gamma \mu_0}{2\pi} \sqrt{[H_{app} + (N_z - N_x)M_s][H_{app} + (N_y - N_x)M_s]},$$

where $\frac{\gamma}{2\pi} = 28$ GHz/T, μ_0 is the magnetic permeability, N_x, N_y, and N_z are the effective demagnetizing factors along the wire's length,
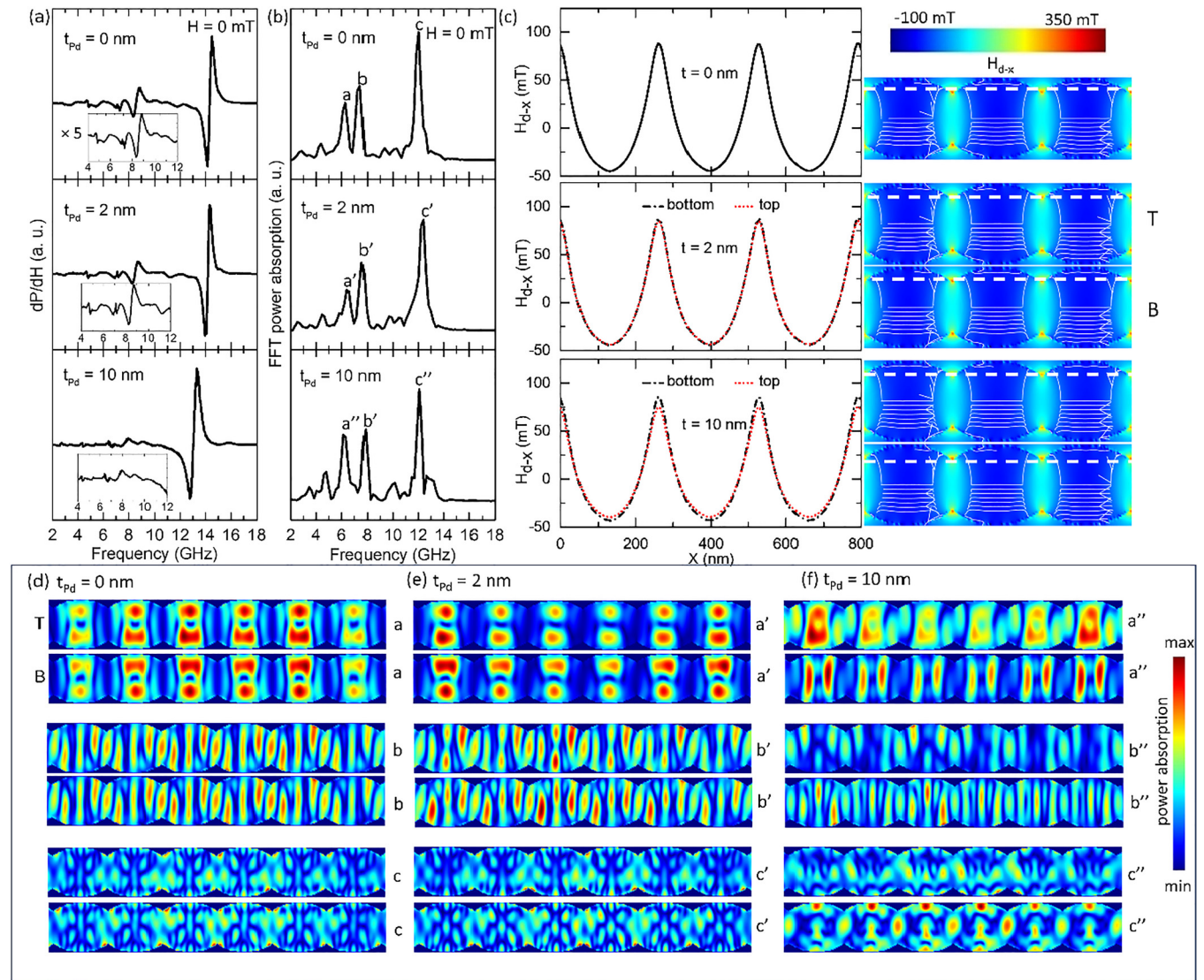
FIG. 2. (a) Experimental and (b) simulated FMR spectra for trilayer WMNW arrays with spacer layer thicknesses $t_{Pd} = 0$, 2, and 10 nm. (c) Spatial variation of the demagnetization field along the x axis and corresponding 2D profiles. Simulated 2D spatial mode profiles corresponding to (d) 0 nm-, (e) 2 nm-, and (f) 10-nm-thick spacer layer in trilayer WMNW samples. "T" indicates the top layer, and "B" indicates the bottom layer. The red color indicates maximum values, and the blue color indicates minimum values.

22 March 2024 09:32:59

width, and thickness, respectively. The FMR spectrum for $t_{Pd} = 0$ nm contains a high-frequency mode at 14.3 GHz, and the spectrum for $t_{Pd} = 2$ nm has a mode at 14.1 GHz. The spectra for $t_{Pd} = 0$ and 2 nm are the same regarding the number of peaks with a slight variation in the frequency position. Furthermore, the spectrum for $t_{Pd} = 10$ nm is different in terms of the number of modes and the frequency position in the frequency range from 4 to 12 GHz. The large intense peak is observed at 13.0 GHz. In addition, the FMR spectra contain several low-intensity modes [insets of Fig. 2(a)] whose frequency is sensitive to t_{Pd}. Unlike uniform demagnetizing field in homogeneous nanowires, the demagnetizing field landscape periodically changes in WMNW arrays. Therefore, multiple low-intensity modes can be attributed to this periodic variation of the demagnetization field (H_d) at constricted and wider regions of the width-modulated nanowires. The number of modes observed is contingent upon the periodicity of the modulation. Our study reveals multiple modes owing to continuous width modulation. In contrast, a recent work detected only two modes arising from spin excitations near the narrower and wider regions of the wire, facilitated by the controlled modulation of the width.[41]

We have plotted the simulated FMR spectra to attribute the multiple modes observed in the experimental FMR spectra, as shown in Fig. 2(b). The most prominent modes observed in the experiment are also found in the simulated FMR spectra. We observe that the number of modes and frequency positions are sensitive to t_{Pd}. For a detailed understanding of the spatial localization of the resonance modes, we have estimated H_d for $t_{Pd} = 0$ nm, 2 nm, and 10 nm WMNW arrays. The line scans of the x component of H_d (H_{d-x}) along the x axis and 2D profiles of the spatial distribution of H_{d-x} at remanence are shown in Fig. 2(c). We have found that H_{d-x} varies non-uniformly along the length of the wire and is the reason for multiple resonance modes in all WMNW arrays. For example, H_{d-x} is relatively higher in the constricted regions than in the bulk part.

The difference in the H_{d-x} at the constricted region and center of the lobe is ~130 mT in all the WMNW arrays. This variation in the demagnetization fields leads to multiple peaks spatially localized at different parts of the wire. The variation in H_{d-x} of the top and bottom layers in $t_{Pd} = 2$ nm is negligible. Like the single-layer sample ($t_{Pd} = 0$ nm), the top and bottom layers in $t_{Pd} = 2$ nm sample show a similar distribution of H_d, suggesting exchange coupling between the layers. However, the variation in H_{d-x} of the top and bottom layers in $t_{Pd} = 10$ nm is ~12 mT. For $t_{Pd} = 10$ nm, the spatial distribution of the top and bottom layers differs due to the dominance of dipolar coupling. To understand the origin of the multiple modes observed in the experimental FMR spectra, we have plotted the 2D spatial mode profiles, as shown in Figs. 2(d)–2(f). In the case of $t_{Pd} = 0$ and 2 nm [Figs. 2(d) and 2(e)], the power absorption in the top and bottom layers is similar, indicating that the two layers are exchange-coupled. The frequency of the resonant mode is contingent upon the effective magnetic field, comprising the external magnetic field, demagnetizing field, and exchange fields. While the effective field remains uniform for a homogeneous wire, it becomes non-uniform in the case of WMNWs due to the presence of an inhomogeneous demagnetizing field. This non-uniformity becomes increasingly pronounced with a reduction in the periodicity of modulation (approximately

265 nm). The continuous modulation in width induces curling of magnetization, particularly in constricted areas. Here, we discuss the three most prominent modes observed in the FMR spectra. In Figs. 2(d) and 2(e), modes a, a' are located at the center of the non-modulated region. Here, a, b, c correspond to the modes in $t_{Pd} = 0$ nm, and a', b', c' correspond to the modes in $t_{Pd} = 2$ nm WMNW arrays. The modes below a and a' can be the edge modes, which require more external fields to align magnetization in the field direction. Therefore, the resonance frequency of the edge mode is less compared to the center modes from Kittel's equation. Due to the continuous width modulation, the demagnetization field is non-uniform along the length of the wire, thus leading to the hybrid modes. Modes b and b' are hybrid in nature, where the power absorption is near the modulated and the non-modulated regions but with different intensities. The highest frequency modes, c, and c', belong to the power absorption at the modulated region. We found that the largest frequency mode belongs to the spin excitations at the narrowest region, whereas the smallest frequency mode belongs to the spin excitations at the widest part of the wire. This is attributed to the increase in demagnetization factor along the y direction with a decrease in nanowire widths. The 2D spatial profiles for modes a'', b'', and c'' of WMNW arrays with $t_{Pd} = 10$ nm are shown in Fig. 2(f). Due to the dipolar coupling, which favors the anti-parallel alignment of magnetization, the power absorption in the top and bottom layers is different, unlike the case in $t_{Pd} = 0$ and 2 nm. The top and bottom layers exhibit independent behavior and show less coherence between them. The mode a'' is predominantly localized at the widest section of the wire in the top layer. Conversely, in the bottom layer, the a'' mode is localized at the widest part of the wire, with minimal excitation occurring at the center. The constituent two magnetic layers of these WMNWs, i.e., 20-nm-thick and 50-nm-thick single-layer nanowires, also possess multiple modes at remanence with a main most-intense Kittel-like mode for uniform magnetization at the central part of the wires (see Fig. S3 in the supplementary material for more information).

To understand the effect of the magnetic field on the microwave response, the FMR spectra are measured at $\theta = 0°$ by varying $\mu_0 H_{app}$ from 0 to 100 mT for $t_{Pd} = 10$ nm, as shown in Fig. 3(a). We detected the high-intense modes at high frequencies and low-intense modes at low frequencies. We have observed that with an increase in H_{app}, resonance frequency (f_{res}) increases, satisfying Kittel's equation. The same behavior is observed for $t_{Pd} = 0$ nm and 2 nm WMNW arrays (see Fig. S4 in the supplementary material for more information). The intensity of the modes found in the frequency range from 4 to 12 GHz became more prominent with an increase in the field. This is due to the enhanced alignment of magnetic moments toward the field direction. We found high intense peaks at $f_{res} = 13.1$, 14.3, 15.1, 15.9, and 16.7 GHz for $\mu_0 H_{app} = 0$, 25, 50, 75, and 100 mT, respectively. We have simulated FMR spectra to validate the experimental results, as shown in Fig. 3(b). The micromagnetic simulations are performed on a WMNW by applying a magnetic field along the wire's long axis and a sinc field perpendicular to it. We have obtained multiple modes in our simulations in agreement with the experimental findings. The high-frequency peaks in the absorption spectra appear at 12.0, 13.1, 13.3, 14.2, and 15.0 GHz, which agree with the experimental findings.
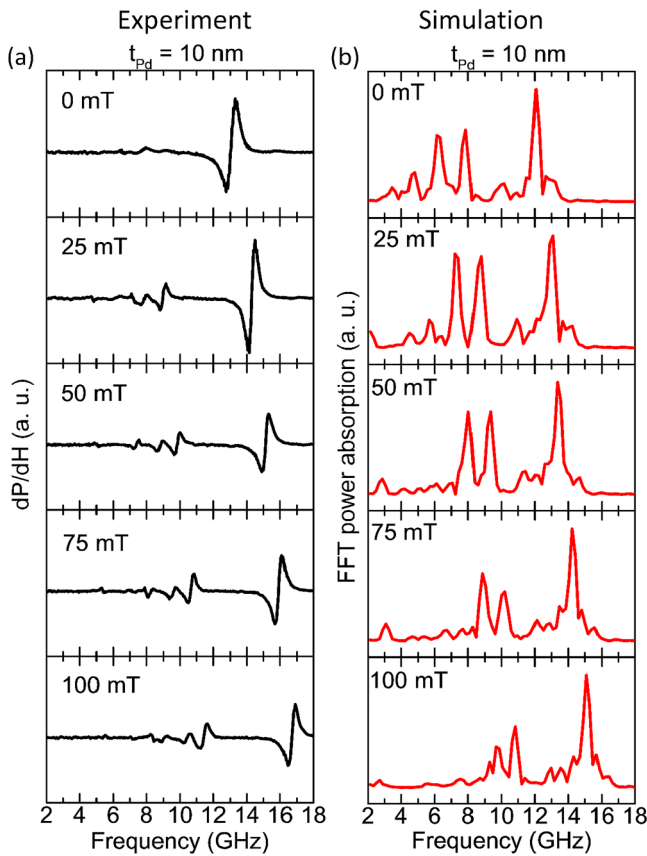
FIG. 3. (a) Experimental and (b) simulated FMR spectra at 0, 25, 50, 75, and 100 mT for the trilayer WMNW sample with t_{Pd} = 10 nm.

FIG. 4. Experimental 2D FMR spectra for trilayer WMNW arrays with spacer layer thickness (a) t_{Pd} = 0 nm (b) t_{Pd} = 2 nm, and (c) t_{Pd} = 10 nm. Simulated 2D FMR spectra for trilayer WMNW arrays with spacer layer thickness (d) t_{Pd} = 0 nm (e) t_{Pd} = 2 nm, and (f) t_{Pd} = 10 nm.

The slight variations in the frequency positions can be due to the rough edges in the patterned modulated wires. The experimental results are qualitatively in good agreement with the simulation results.

To illustrate the Kittel-type resonant mode variations across the reversal regime, we have studied the FMR absorption spectra by varying $\mu_0 H_{app}$ from +50 to −50 mT for all the WMNW arrays. The two-dimensional (2D) FMR spectra obtained from both experimental and simulated data are presented in Fig. 4. We observe two colors corresponding to maximum and minimum intensities at the resonant mode spectra, as the measured signal is an anti-derivative. Notably, WMNW arrays exhibit multiple resonance modes attributable to the non-uniform demagnetizing field. Furthermore, we have observed that the frequency variation across the magnetization switching regime for all modes strongly correlates with the thickness of the spacer layer. Specifically, in the case of t_{Pd} = 0 nm, the resonance frequency steadily decreases with the applied field until −16 mT. A noteworthy occurrence is the sharp frequency jump from 13.8 to 14.9 GHz observed around −16 mT for the most intense Kittel-type mode. In the case of t_{Pd} = 0 nm, f_{res} monotonically decreases with the applied field till −16 mT, and a sharp
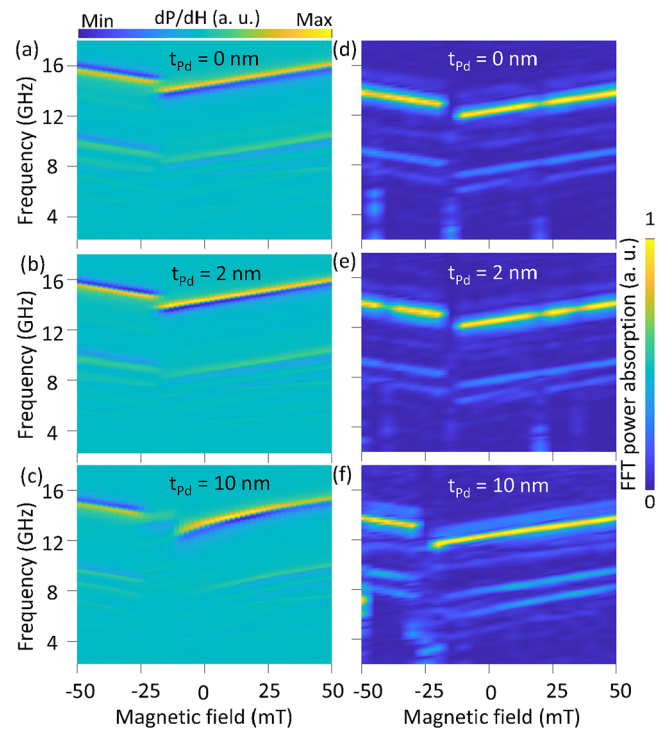
frequency jump from 13.8 to 14.9 GHz is observed around −16 mT for the most intense Kittel-type mode. f_{res} then starts to increase monotonically in the negative saturation region as magnetization starts to align in the −x direction. This behavior can be correlated with observations in the magnetization reversal curves, as shown in Fig. 1(c). A similar sharp frequency jump is observed for the less intense modes as well. Similarly, in Fig. 4(b) for t_{Pd} = 2 nm, there is a noticeable frequency jump from 13.6 to 14.7 GHz around −18 mT for the most intense Kittel-type mode. This is consistent with the hysteresis loop for t_{Pd} = 2 nm, as Fig. 1(c) shows. A similar sharp frequency jump is observed in the single-layer WMNW arrays (see Fig. S5 in the supplementary material for more information). Figure 4(c) shows the f_{res} vs H_{app} plot for the WMNW array with t_{Pd} = 10 nm. We observed a gradual increase of f_{res} from 12.3 GHz ($\mu_0 H_{app}$ = −9.5 mT) to 14 GHz ($\mu_0 H_{app}$ = −22 mT) for the most intense Kittel-type mode. For $\mu_0 H_{app}$ = −9.5 mT to −22 mT, we have observed less intense modes that does not satisfy Kittel's equation. Kittel's equation explains the uniform magnetization oscillations for the saturated states, and the behavior of the f_{res} vs H_{app} curve is monotonic. Hence, the regime where the curve is non-monotonic and does not follow the Kittel fit corresponds to the non-parallel alignment of magnetization of the top and bottom layers. This agrees with the hysteresis loop [Fig. 1(c)], where the two peaks are observed due to the independent switching of

22 March 2024 09:32:59

magnetization in both layers. Non-smooth switching is also observed for the less intense modes. This is due to the drastic change in the magnetization configuration during the reversal process. Here, we emphasize that the modulation of the width and change in thickness of the wire has increased the number of modes. Meanwhile, the jump in frequency (sharp or gradual) solely depends on the spacer layer thickness. For a deeper comprehension of the experimental FMR results, we conducted simulations of FMR spectra, as depicted in Figs. 4(d)–4(f). Notably, there exists good qualitative agreement between the resonant modes observed experimentally and those simulated. However, quantitatively, there is a discrepancy of approximately 2 GHz between the experimental and simulation results. This divergence arises because the simulations were conducted on single isolated nanowires, thus remaining uncoupled, while the experimental setup involved a large array of nanowires where factors such as inhomogeneity, edge roughness, and size distribution influenced the microwave response. The simulated spectra for $t_{Pd} = 0$ and 2 nm exhibit sharp switching for all modes, indicating a single-layer-like behavior in the trilayer with $t_{Pd} = 2$ nm, as illustrated in Figs. 4(d) and 4(e). Conversely, for $t_{Pd} = 10$ nm, there is an abrupt frequency jump, particularly pronounced for low-frequency modes, attributable to the dipolar coupling between the ferromagnetic layers.

To demonstrate the influence of shape anisotropy on the spin dynamics, we have recorded f_{res} as a function of field angle θ and t_{Pd}; the results are summarized in Fig. 5. Note that the extracted values of f_{res} are obtained from the FMR spectra measured at 75 mT (see Fig. S6 in the supplementary material for more information). The easy and hard axes of the nanowires correspond to $\theta = 0°$ and 90°, respectively. We have observed a decrease in f_{res} with an increase in θ from 0° to 90° for all the spacer layer thicknesses. For instance, with an increase in θ from 0° to 60°, f_{res} values are from 16.6 to 15.2 GHz for $t_{Pd} = 0$ nm, 16.5–14.9 GHz for
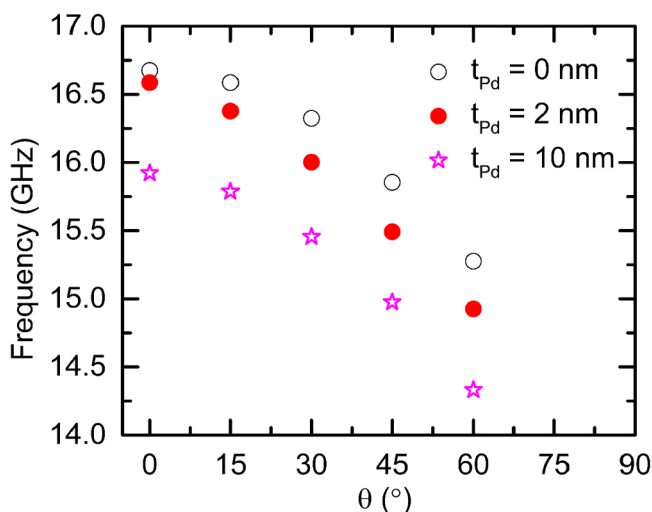
$t_{Pd} = 2$ nm, and 15.9–14.3 GHz for $t_{Pd} = 10$ nm WMNW arrays, due to a change in demagnetizing field landscape. The demagnetization factor along the x direction is minimum at $\theta = 0°$ and maximum at $\theta = 90°$. Hence, when the field orientation deviates from the easy axis, f_{res} decreases and vice versa. We were unable to detect FMR modes near the hard axis region (for $\theta > 60°$) due to the insufficient saturation of the nanowire at 75 mT [given on the constraint on frequency range in our FMR experiment (up to 18 GHz), we have chosen 75 mT]. From the hysteresis loop of $\theta = 90°$ [Fig. 1(d)], it is clear that the sample requires more than 200 mT to saturate magnetization.

CONCLUSION

We have investigated the magnetization reversal processes and dynamic properties of trilayered Py nanowires with periodic width modulation and compared them with single-layer nanowires. We observed that the type of coupling between the ferromagnetic layers changed from exchange to dipolar when the spacer layer thickness increased from 2 to 10 nm. This affected the magnetization switching: nanowires with a 2-nm-thick spacer layer switched sharply, similar to single-layer nanowires, because of the strong exchange coupling. Nanowires with a 10-nm-thick spacer layer switched in two steps because of weaker dipolar coupling. We also found that the spacer layer thickness influenced the ferromagnetic resonance spectra, which showed different numbers and values of modes and frequencies. This was due to the different magnetization configurations for different spacer layer thicknesses. We observed a sudden change in frequency from 13.6 to 14.7 GHz around −18 mT in the trilayer WMNW array with $t_{Pd} = 2$ nm, which matched the single-layer WMNW array. We saw a non-smooth behavior in the field range −9.5 to −22 mT in the trilayer sample with $t_{Pd} = 10$ nm because of the dipolar coupling between the ferromagnetic layers. The dynamic responses in this spin-valve-type structure are useful for designing microwave-based spintronic devices.

SUPPLEMENTARY MATERIAL

See the supplementary material for the analysis of hysteresis loops and ferromagnetic resonance spectra of single-layer width-modulated nanowires; simulated hysteresis loops, field, and angle dependent ferromagnetic resonance spectra of trilayer width-modulated nanowires.

FIG. 5. Resonance frequencies vs field orientation as a function of spacer layer thickness at $\mu_0 H_{app} = 75$ mT.

AUTHOR DECLARATIONS

Conflict of Interest

The authors have no conflicts to disclose.

Author Contributions

Mahathi Kuchibhotla: Data curation (equal); Formal analysis (equal); Investigation (equal); Writing – original draft (lead). **Arabinda Haldar:** Conceptualization (equal); Funding acquisition (equal); Investigation (equal); Project administration (equal); Supervision (equal); Writing – review & editing (equal). **Adekunle Olusola Adeyeye:** Conceptualization (equal); Funding acquisition (equal); Investigation (equal); Project administration (equal); Supervision (equal); Writing – review & editing (equal).

DATA AVAILABILITY

The data that support the findings of this study are available within the article and its supplementary material.

REFERENCES

[1]A. Barman, G. Gubbiotti, S. Ladak, A. O. Adeyeye, M. Krawczyk, J. Gräfe, C. Adelmann, S. Cotofana, A. Naeemi, V. I. Vasyuchka, B. Hillebrands, S. A. Nikitov, H. Yu, D. Grundler, A. V. Sadovnikov, A. A. Grachev, S. E. Sheshukova, J. Y. Duquesne, M. Marangolo, G. Csaba, W. Porod, V. E. Demidov, S. Urazhdin, S. O. Demokritov, E. Albisetti, D. Petti, R. Bertacco, H. Schultheiss, V. V. Kruglyak, V. D. Poimanov, S. Sahoo, J. Sinha, H. Yang, M. Münzenberg, T. Moriyama, S. Mizukami, P. Landeros, R. A. Gallardo, G. Carlotti, J. V. Kim, R. L. Stamps, R. E. Camley, B. Rana, Y. Otani, W. Yu, T. Yu, G. E. W. Bauer, C. Back, G. S. Uhrig, O. V. Dobrovolskiy, B. Budinska, H. Qin, S. Van Dijken, A. V. Chumak, A. Khitun, D. E. Nikonov, I. A. Young, B. W. Zingsem, and M. Winklhofer, "The 2021 magnonics roadmap," J. Phys. Condens. Matter **33**, 413001 (2021).

[2]B. Lenk, H. Ulrichs, F. Garbs, and M. Münzenberg, "The building blocks of magnonics," Phys. Rep. **507**, 107 (2011).

[3]A. V. Chumak, P. Kabos, M. Wu, C. Abert, C. Adelmann, A. O. Adeyeye, J. Akerman, F. G. Aliev, A. Anane, A. Awad, C. H. Back, A. Barman, G. E. W. Bauer, M. Becherer, E. N. Beginin, V. A. S. V. Bittencourt, Y. M. Blanter, P. Bortolotti, I. Boventer, D. A. Bozhko, S. A. Bunyaev, J. J. Carmiggelt, R. R. Cheenikundil, F. Ciubotaru, S. Cotofana, G. Csaba, O. V. Dobrovolskiy, C. Dubs, M. Elyasi, K. G. Fripp, H. Fulara, I. A. Golovchanskiy, C. Gonzalez-Ballestero, P. Graczyk, D. Grundler, P. Gruszecki, G. Gubbiotti, K. Guslienko, A. Haldar, S. Hamdioui, R. Hertel, B. Hillebrands, T. Hioki, A. Houshang, C. M. Hu, H. Huebl, H. Huth, E. Iacocca, M. B. Jungfleisch, G. N. Kakazei, A. Khitun, R. Khymyn, T. Kikkawa, M. Klaui, O. Klein, J. W. Klos, S. Knauer, S. Koraltan, M. Kostylev, M. Krawczyk, I. N. Krivorotov, V. V. Kruglyak, D. Lachance-Quirion, S. Ladak, R. Lebrun, Y. Li, M. Lindner, R. Macêdo, S. Mayr, G. A. Melkov, S. Mieszczak, Y. Nakamura, H. T. Nembach, A. A. Nikitin, S. A. Nikitov, V. Novosad, J. A. Otalora, Y. Otani, A. Papp, B. Pigeau, P. Pirro, W. Porod, F. Porrati, H. Qin, B. Rana, T. Reimann, F. Riente, O. Romero-Isart, A. Ross, A. V. Sadovnikov, A. R. Safin, E. Saitoh, G. Schmidt, H. Schultheiss, K. Schultheiss, A. A. Serga, S. Sharma, J. M. Shaw, D. Suess, O. Surzhenko, K. Szulc, T. Taniguchi, M. Urbanek, K. Usami, A. B. Ustinov, T. Van Der Sar, S. Van Dijken, V. I. Vasyuchka, R. Verba, S. V. Kusminskiy, Q. Wang, M. Weides, M. Weiler, S. Wintz, S. P. Wolski, and X. Zhang, "Advances in magnetics roadmap on spin-wave computing," IEEE Trans. Magn. **58**(6), 0800172 (2022).

[4]A. V. Chumak, V. I. Vasyuchka, A. A. Serga, and B. Hillebrands, "Magnon spintronics," Nat. Phys. **11**, 453 (2015).

[5]A. V. Chumak, A. A. Serga, and B. Hillebrands, "Magnon transistor for all-magnon data processing," Nat. Commun. **5**, 4700 (2014).

[6]A. A. Nikitin, A. B. Ustinov, A. A. Semenov, A. V. Chumak, A. A. Serga, V. I. Vasyuchka, E. Lähderanta, B. A. Kalinikos, and B. Hillebrands, "A spin-wave logic gate based on a width-modulated dynamic magnonic crystal," Appl. Phys. Lett. **106**, 102405 (2015).

[7]S. J. Hämäläinen, M. Madami, H. Qin, G. Gubbiotti, and S. van Dijken, "Control of spin-wave transmission by a programmable domain wall," Nat. Commun. **9**, 4853 (2018).

[8]K. Zhu, M. Carpentieri, L. Zhang, B. Fang, J. Cai, R. Verba, A. Giordano, V. Puliafito, B. Zhang, G. Finocchio, and Z. Zeng, "Nonlinear amplification of microwave signals in spin-torque oscillators," Nat. Commun. **14**, 2183 (2023).

[9]A. Haldar and A. O. Adeyeye, "Deterministic control of magnetization dynamics in reconfigurable nanomagnetic networks for logic applications," ACS Nano **10**, 1690–1698 (2016).

[10]D. G. Krawczyk, "Review and prospects of magnonic crystals and devices with reprogrammable band structure," J. Phys.: Condens. Matter **26**, 123202 (2014).

[11]J. C. Gartside, A. Vanstone, T. Dion, K. D. Stenning, D. M. Arroo, H. Kurebayashi, and W. R. Branford, "Reconfigurable magnonic mode-hybridisation and spectral control in a bicomponent artificial spin ice," Nat. Commun. **12**, 2488 (2021).

[12]A. Haldar, D. Kumar, and A. O. Adeyeye, "A reconfigurable waveguide for energy efficient transmission and local manipulation of information in a nano-magnetic device," Nat. Nanotech. **11**, 437–443 (2016).

[13]J. C. Gartside, S. G. Jung, S. Y. Yoo, D. M. Arroo, A. Vanstone, K. D. Stenning, T. Dion, and W. R. Branford, "Current-controlled nanomagnetic writing for reconfigurable magnonic crystals," Commun. Phys. **3**, 219 (2020).

[14]G. Duerr, M. Madami, S. Neusser, S. Tacchi, G. Gubbiotti, G. Carlotti, and D. Grundler, "Spatial control of spin-wave modes in $Ni_{80}Fe_{20}$ antidot lattices by embedded Co nanodisks," Appl. Phys. Lett. **99**, 202502 (2011).

[15]A. V. Chumak, A. A. Serga, and B. Hillebrands, "Magnonic crystals for data processing," J. Phys. D: Appl. Phys. **50**, 244001 (2017).

[16]J. Topp, D. Heitmann, M. P. Kostylev, and D. Grundler, "Making a reconfigurable artificial crystal by ordering bistable magnetic nanowires," Phys. Rev. Lett. **104**, 207205 (2010).

[17]G. Gubbiotti, X. Zhou, A. O. Adeyeye, G. Varvaro, and M. Kostylev, "Effect of exchange and dipolar interlayer interactions on the magnonic band structure of dense Fe/Cu/Py nanowires with symmetric and asymmetric layer widths," Phys. Rev. B **101**, 224431 (2020).

[18]S. K. Kim, K. S. Lee, and D. S. Han, "A gigahertz-range spin-wave filter composed of width-modulated nanostrip magnonic-crystal waveguides," Appl. Phys. Lett. **95**, 082507 (2009).

[19]J. Rychły-Gruszecka, J. Walowski, C. Denker, T. Tubandt, M. Münzenberg, and J. W. Kłos, "Shaping the spin wave spectra of planar 1D magnonic crystals by the geometrical constraints," Sci. Rep. **12**, 20678 (2022).

[20]S. Saha, S. Barman, Y. Otani, and A. Barman, "All-optical investigation of tunable picosecond magnetization dynamics in ferromagnetic nanostripes with a width down to 50 nm," Nanoscale **7**, 18312 (2015).

[21]M. Kuchibhotla, A. Talapatra, and A. Haldar, "Field orientation dependent magnetization reversal and dynamics in sub-100 nm wide permalloy nanowires," J. Phys. D: Appl. Phys. **55**, 335001 (2022).

[22]F. Lisiecki, J. Rychły, P. Kuświk, H. Głowiński, J. W. Kłos, F. Groß, I. Bykova, M. Weigand, M. Zelent, E. J. Goering, G. Schütz, G. Gubbiotti, M. Krawczyk, F. Stobiecki, J. Dubowik, and J. Gräfe, "Reprogrammability and scalability of magnonic Fibonacci quasicrystals," Phys. Rev. Appl. **11**, 054003 (2019).

[23]J. Topp, G. Duerr, K. Thurner, and D. Grundler, "Reprogrammable magnonic crystals formed by interacting ferromagnetic nanowires," Pure Appl. Chem. **83**, 1989 (2011).

[24]J. Ding, M. Kostylev, and A. O. Adeyeye, "Magnonic crystal as a medium with tunable disorder on a periodical lattice," Phys. Rev. Lett. **107**, 047205 (2011).

[25]P. Lupo, Z. Haghshenasfard, M. G. Cottam, and A. O. Adeyeye, "Ferromagnetic resonance study of interface coupling for spin waves in narrow NiFe/Ru/NiFe multilayer nanowires," Phys. Rev. B **94**, 214431 (2016).

[26]S. Ikeda, K. Miura, H. Yamamoto, K. Mizunuma, H. D. Gan, M. Endo, S. Kanai, J. Hayakawa, F. Matsukura, and H. Ohno, "A perpendicular-anisotropy CoFeB–MgO magnetic tunnel junction," Nat. Mater. **9**, 721 (2010).

[27]Y. Tserkovnyak, A. Brataas, and G. E. W. Bauer, "Spin pumping and magnetization dynamics in metallic multilayers," Phys. Rev. B **66**, 224403 (2002).

[28]Y. Liu, Z. Lan, Z. Yu, R. Guo, X. Jiang, C. Wu, and K. Sun, "Modulation of PSSW resonance field affected by exchange stiffness A in Fe/NiFe/Fe multi-layer films with different Fe film thicknesses," J. Magn. Magn. Mater. **514**, 167222 (2020).

[29]G. Gubbiotti, H. T. Nguyen, R. Hiramatsu, S. Tacchi, M. Madami, M. G. Cottam, and T. Ono, "Field dependence of the magnetic eigenmode frequencies in layered nanowires with ferromagnetic and antiferromagnetic ground states: Experimental and theoretical study," J. Phys. D: Appl. Phys. **47**, 365001 (2014).

[30]C. Luo, Y. Yin, D. Zhang, S. Jiang, J. Yue, Y. Zhai, J. Du, and H. Zhai, "Effect of spacer layer on the magnetization dynamics of permalloy/rare-earth/permalloy trilayers," J. Appl. Phys. **117**, 17D124 (2015).

[31]G. Gubbiotti, X. Zhou, Z. Haghshenasfard, M. G. Cottam, and A. O. Adeyeye, "Reprogrammable magnonic band structure of layered permalloy/Cu/permalloy nanowires," Phys. Rev. B **97**, 134428 (2018).

[32]G. Gubbiotti, X. Zhou, Z. Haghshenasfard, M. G. Cottam, A. O. Adeyeye, and M. Kostylev, "Interplay between intra- and inter-nanowires dynamic dipolar interactions in the spin wave band structure of Py/Cu/Py nanowires," Sci. Rep. **9**, 4617 (2019).

[33]K. S. Lee, D. S. Han, and S. K. Kim, "Physical origin and generic control of magnonic band gaps of dipole-exchange spin waves in width-modulated nano-strip waveguides," Phys. Rev. Lett. **102**, 127202 (2009).

[34]A. Adhikari, C. Banerjee, A. Kumar Mondal, A. Kumar Chaurasiya, S. Choudhury, J. Sinha, S. Barman, and A. Barman, "Anisotropic spin-wave propagation in asymmetric width modulated $Ni_{80}Fe_{20}$ nanostripes," Mater. Sci. Eng. B **272**, 115385 (2021).

[35]S. Lepadatu, O. Wessely, A. Vanhaverbeke, R. Allenspach, A. Potenza, H. Marchetto, T. R. Charlton, S. Langridge, S. S. Dhesi, and C. H. Marrows, "Domain-wall spin-torque resonators for frequency-selective operation," Phys. Rev. B **81**, 060402 (2010).

[36]A. V. Chumak, P. Pirro, A. A. Serga, M. P. Kostylev, R. L. Stamps, H. Schultheiss, K. Vogt, S. J. Hermsdoerfer, B. Laegel, P. A. Beck, and B. Hillebrands, "Spin-wave propagation in a microstructured magnonic crystal," Appl. Phys. Lett. **95**, 262508 (2009).

[37]F. Ciubotaru, A. V. Chumak, N. Yu Grigoryeva, A. A. Serga, and B. Hillebrands, "Magnonic band gap design by the edge modulation of micro-sized waveguides," J. Phys. D: Appl. Phys. **45**, 255002 (2012).

[38]A. O. Adeyeye and N. Singh, "Large area patterned magnetic nanostructures," J. Phys. D: Appl. Phys. **41**, 153001 (2008).

[39]A. Vansteenkiste, J. Leliaert, M. Dvornik, M. Helsen, F. Garcia-Sanchez, and B. Van Waeyenberge, "The design and verification of MuMax3," AIP Adv. **4**, 107133 (2014).

[40]D. Kumar and A. O. Adeyeye, "Techniques in micromagnetic simulation and analysis," J. Phys. D: Appl. Phys. **50**, 343001 (2017).

[41]G. Gubbiotti, L. L. Xiong, F. Montoncello, L. Giovannini, and A. O. Adeyeye, "Spin wave dispersion and intensity correlation in width-modulated nanowire arrays: A Brillouin light scattering study," J. Appl. Phys. **124**, 083903 (2018).